Cell, Vol. 116, 737–749, March 5, 2004, Copyright ©2004 by Cell Press

The Mechanism of Myosin VI Translocation and Its Load-Induced Anchoring

David Altman,[1] H. Lee Sweeney,[2] and James A. Spudich[3,*]

[1]Department of Physics
Stanford University
Stanford, California 94305

[2]Department of Physiology
University of Pennsylvania School of Medicine
Philadelphia, Pennsylvania 19104

[3]Department of Biochemistry
Stanford University School of Medicine
Stanford, California 94305

Summary

Myosin VI is thought to function as both a transporter and an anchor. While in vitro studies suggest possible mechanisms for processive stepping, a biochemical basis for anchoring has not been demonstrated. Using optical trapping, we observed myosin VI stepping against applied forces. Step size is not strongly affected by such loads. At saturating ATP, myosin VI kinetics shows little dependence on load until, at forces near stall, its stepping slows dramatically as load increases. At subsaturating ATP or in the presence of ADP, stepping kinetics is significantly inhibited by load. From our results, we propose a mechanism of myosin VI stepping that predicts a regulation through load of the motor's roles as transporter and anchor.

Introduction

Myosin VI is hypothesized to perform both roles as a transporter and an anchor. As a transporter, the motor is implicated in carrying proteins to the leading edge of a migrating cell (Buss et al., 2002) and moving endocytic vesicles into a cell (Buss et al., 2001b). As an anchor, it may link actin-regulatory proteins to an actin complex during *Drosophila* spermatogenesis (Fabrizio et al., 1998; Rogat and Miller, 2002) and moor stereocilia to the hair cell of inner ear sensory epithelia (Hasson et al., 1997). The motor may also behave as a dynamic tension sensor, translocating along actin to establish tension in a system and then anchoring to the filament to maintain this tension. To behave as an anchor, the motor must remain bound to an actin filament through its catalytic domains, anchoring to actin whatever is associated to its tail. The mechanisms by which myosin VI functions as a processive motor and an anchor are not understood, nor how the motor regulates which function is exhibited. We address these questions using single molecule assays that probe effects of applied external forces, or loads, on motor stepping.

Studies of motor proteins have been aided by tools such as optical traps (Block et al., 2003; Mehta et al., 1999; Wang et al., 1998) and glass micro-needles (Ishijima et al., 1994), which allow for observation of individual motors. Whereas information about intermediate states is averaged out in bulk protein studies, single molecule assays allow for observation of microscopic rates within a motor's kinetic cycle. An especially useful approach has been to apply a load to an active motor. Applied forces selectively perturb mechanical transitions, and so observed effects on activity single out these steps in the chemomechanical cycle (Block et al., 2003; Wang et al., 1998).

The stepping mechanism for processive myosins has been most thoroughly studied with myosin V. A popular scheme to explain the stepping of this motor is the lever arm model, which predicts that small changes in the catalytic head of the motor are amplified to large, directed displacements through a relatively rigid lever arm (Purcell et al., 2002; Sakamoto et al., 2003; Spudich, 2001). For myosin V, each catalytic domain is followed by six light chain binding motifs that serve as the motor's lever arm, enabling it to span its 36 nm step.

Myosin VI, also a processive motor (Rock et al., 2001), is the only characterized myosin to move predominantly toward the pointed end of actin. This directionality is hypothesized to arise from a rotation of the motor's putative lever arm (Wells et al., 1999). Following the myosin VI catalytic head is a 50 amino acid insert recently shown to bind calmodulin (Bahloul et al., 2004), and following this insert is an IQ domain that also binds a calmodulin light chain. Together, these two regions may form a lever arm consisting of two bound light chains that, according to the lever arm model, could account for a step size of ~10 nm. In agreement with this, we have recently used laser trap analysis to measure the stroke size of a single-headed myosin VI construct to be ~12 nm (R. Rock and A. Dunn, personal communication).

Recent studies, however, show that myosin VI takes a step of ~30 nm, too large to be explained simply by a lever arm mechanism. Myosin VI stepping also differs from myosin V in the variability of its step size. The standard deviation of a myosin VI step distribution is twice that of myosin V, suggesting that it may have a larger diffusive character to its stepping relative to myosin V. Myosin VI also undergoes a considerable number of backward steps, behavior not frequently observed with myosin V (Rock et al., 2001).

Though a stroke involving its short lever arm may influence the predominant direction of myosin VI stepping, an alternative stepping model is required to explain its large diffusive steps. One proposed model is that an interaction between the motor and actin causes a conformational change in the actin track. This change allows the motor to slide along the track in a manner not envisaged by conventional models of stepping (Nishikawa et al., 2002). Another model is that myosin VI undergoes multiple small steps for each ATP hydrolysis. This suggestion would be unique from the usual relationship observed for myosins in which a single step is tightly coupled with a single ATP hydrolysis (Finer et al., 1994; Rief et al., 2000; Veigel et al., 1999).

If we assume the actin is relatively unaffected and the

*Correspondence: jspudich@stanford.edu

motor exhibits a one-to-one ratio between stepping and ATP hydrolysis, a conformational change in myosin VI must occur that allows it to span ~30 nm. A mechanism in which some part of the motor extends and becomes flexible is a plausible explanation for the observed behavior. An extended, flexible element would allow the motor to span a large step and diffusively reach numerous actin monomers surrounding its usual binding site, leading to a wide distribution in step size and occasional backward stepping. A motor whose stepping mechanism involves a large diffusive search may also be more likely to bind different actin filaments to each head. Thus, this unique stepping mechanism may dictate specific in vivo functions of myosin VI.

If the mechanical transition for myosin VI involves an extended, flexible element, load effects on kinetics should differentiate its stepping scheme from that of myosin V, which undergoes its mechanical transition with relatively rigid arms. Here, we describe effects of applied load on myosin VI and propose a mechanism for its stepping.

Studying load-affected kinetics can also yield information about the mechanism of anchoring by myosin VI. A load applied against a motor's motion forces it to do additional work to undergo mechanical transitions. This results in a slowing of the rates describing these transitions and thus can also slow overall stepping. A processive motor experiencing a load could thus function as an anchor if, under sufficient backward force, its stepping kinetics slows to a halt while it remains bound to actin. We explored effects of backward forces on the stepping of myosin VI to test whether this is the biochemical basis for its anchoring.

According to our current model for the myosin VI stepping cycle, the trailing head of the myosin VI dimer is strongly bound to actin in an ADP state, releases its ADP to allow ATP to bind, and releases from actin upon ATP association. The head then traverses ~30 nm and rebinds to actin after hydrolyzing ATP and releasing phosphate, positioning itself as the new lead head. The new trailing head then repeats the cycle identically.

This stepping cycle is represented by the following model showing the nucleotide and actin bound states of the motor:

$$A \bullet MD \underset{[ADP]k_{-1}}{\overset{k_{+1}}{\leftrightarrow}} A \bullet M \underset{k_{-2}}{\overset{[ATP]k_{+2}}{\leftrightarrow}} MT \underset{k_{-3}}{\overset{k_{+3}}{\leftrightarrow}} MDP_i \underset{[P_i]k_{-4}}{\overset{k_{+4}}{\leftrightarrow}} A \bullet MD. \quad (1)$$

k_{+i} are rates in the forward (rightward) direction, and k_{-i} are rates in the opposite direction. *M* denotes the myosin VI head and *A* • *M* indicates that it is strongly bound to actin. *D*, *DP*$_i$, and *T* represent the ADP, ADP•P$_i$, and ATP states of the motor, respectively. The cycle begins on the left with *M* representing the trailing myosin VI head in an ADP state and strongly bound to actin. When this head reaches the right side of this model, it has become the lead head. The new trailing head continues the cycle on the left again, starting in its ADP actin bound state.

According to this model, there are three likely ways in which load could affect the nucleotide-dependent kinetics and cause the motor to anchor to an actin filament: load could slow release of ADP from the trailing myosin VI head (k_{+1}), slow association of ATP to this head (k_{+2}), or increase the rate of ADP binding to this head (k_{-1}) and thus compete with binding of ATP. We have characterized the effects of load on these rates and observe a reduction in the ATP on rate and an increase in the ADP on rate as load increases. At physiological conditions, however, the latter effect is most relevant to motor function. Thus, a load-induced increase in ADP association to the trailing head is the likely mechanism for switching myosin VI function from that of a translocator to an anchor.

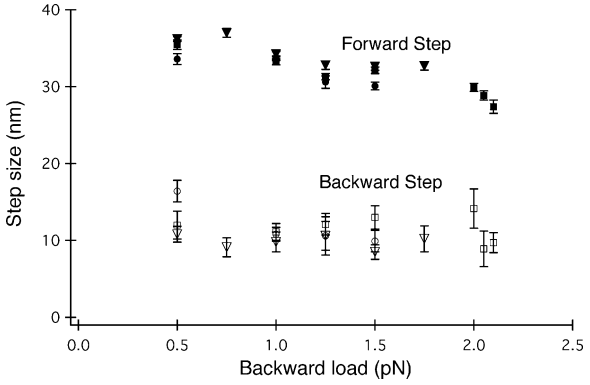

Figure 1. Dependence of Step Size on Load

Mean forward step in the presence of 2 mM ATP (■), 100 μM ATP (▼), and 1.5 mM ATP and 1 μM ADP (●), and mean backward step in the presence of 2 mM ATP (□), 100 μM ATP (▽), and 1.5 mM ATP and 1 μM ADP (○) as functions of load. Errors are standard error of the mean (SEM). Because step distributions are Gaussian (data not shown), SEM is the standard deviation divided by the square root of the number of steps, N. The N for each condition is presented in Supplemental Data on the *Cell* website.

For distributions collected at 2 mM ATP, an Analysis of Variance (ANOVA) test confirmed that load has a significant effect on forward mean step size ($F(6, 2663) = 18.081$, $p < 0.0001$). Similarly, though there may be a small decrease from 0.5 to 1 pN load, the effect of load on backward step size is not significant for loads of 1 pN to 2.1 pN ($F(5, 82) = 0.905$, $p = 0.4820$). Load also has little effect on the frequency of backward steps as shown by a χ^2 test with null hypothesis: $\rho_1 = \rho_2 = \ldots = \rho_7$, where ρ_i is the probability of a backward step at load F_i; $p = 0.51$, $N = 7$. The mean percentage of steps that are backward at saturating ATP over all loads is 3.9% ± 0.1% (mean ± SEM, $N = 7$).

Results

At Saturating ATP, Step Size Is Not Strongly Affected by Load and Kinetic Activity Is Unaffected by Load until High Forces

Dual optical trap assays were used to observe stepping of individual motors against constant loads (see Experimental Procedures). The predominant direction of myosin VI stepping is denoted as *forward* and the opposite direction as *backward*. All loads described here are backward.

The observed step size of myosin VI at saturating (2 mM) ATP shows a weak dependence on load (Figure 1). There is a small but significant change in forward mean step size, from 35 nm near zero load to 27 nm near stalling loads (~2.2 pN). Along a face of an actin filament, adjacent actin monomers along one long-pitch

helix are separated by 5.5 nm (Sheterline and Sparrow, 1994). This decrease of ~8 nm thus may be due to the myosin binding to a site that is at most two actin monomers short of its most frequent unloaded binding site.

The backward step does not change significantly with varying load and, at loads of 1 pN and higher, remains constant at 11 nm. Furthermore, loads do not change the frequency of backward stepping relative to forward stepping. The percentage of steps in the backward directions remains at 4% over all loads (Figure 1 legend).

Information about the motor's stepping kinetics is inferred from measured dwell times, defined as the time between consecutive translocations (Figure 7B). An observed dwell, τ, is the duration of a single catalytic cycle, and so mean dwell, $\bar{\tau}$, is the inverse of the mean stepping rate, $\bar{v}^{-1}$.

At saturating ATP, the mean dwell of myosin VI is not strongly load dependent until forces approaching its stall (Figure 2A). The mean dwell remains fairly constant at ~0.3 s until forces greater than 2 pN are reached. At these high loads, increasing load causes the motor's stepping to slow dramatically.

At Saturating ATP, the Unloaded Stepping Cycle Is Dominated by Biochemical Transitions and Contains a Rapid Mechanical Step

If we consider the energy landscape model of kinetics (Wang et al., 1998), and assume the myosin VI chemomechanical cycle consists of a series of biochemical steps and a single load-dependent mechanical transition the mean dwell of the motor is expected to obey a Boltzmann-type relation:

$$\bar{\tau} = \tau_b + \tau_m \times \exp\left(\frac{F\delta}{k_B T}\right) \quad (2)$$

where F is the applied backward load, δ is the distance over which the load acts, $k_B T$ is the thermal energy, and $\tau_b/(\tau_b + \tau_m)$ and $\tau_m/(\tau_b + \tau_m)$ represent the fraction of time the unloaded motor spends undergoing biochemical and mechanical transitions within its catalytic cycle.

Fitting Equation 2 to the mean dwells observed at saturating ATP yields $\tau_b/(\tau_b + \tau_m) \approx 1$ and $\tau_m/(\tau_b + \tau_m) \approx 0$ (Figure 2A). Thus, at low loads the mechanical transition occurs rapidly compared to the overall cycle time. Because only two data points describe the rapid rise in dwell time at high loads, the fit value for δ, denoted δ_1, of 90 nm is approximate. This could account for the value being larger than the motor's step size, or alternatively, the motor could move forward against load a distance larger than its step and then move backward again. Nonetheless, the rapid rise in mean dwell at $\geq$2 pN suggests δ_1 is large, presumably on the order of the step size.

Our assumption that the motor's chemomechanical cycle contains a single mechanical transition is consistent with a large value for δ_1 (Fisher and Kolomeisky, 1999). For cycles involving numerous mechanical transitions, each with a δ smaller than the step, mean dwell is typically expected to rise less rapidly with increasing load. Specific kinetic schemes involving multiple mechanical transitions, however, can also allow for a δ on the order of the step size. We assume in this manuscript that the large δ_1 is due to a single mechanical transition.

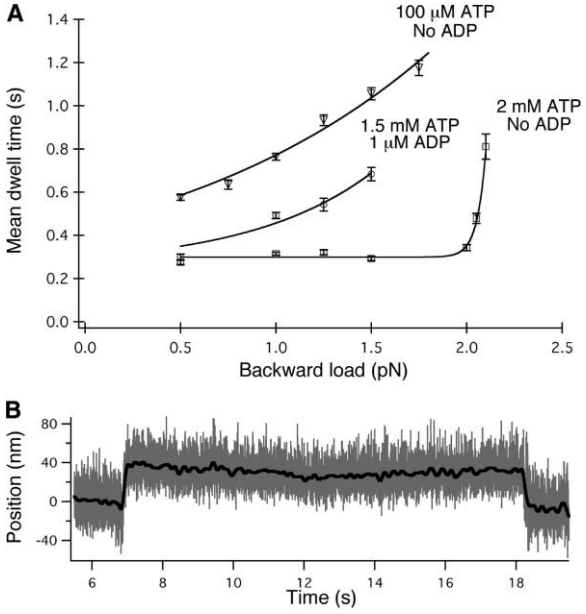

Figure 2. Dependence of Mean Dwell Time on Load

(A) Mean dwell time as a function of load in the presence of 2 mM ATP (□), 100 μM ATP (▽), and 1.5 mM ATP and 1 μM ADP (○). Because dwell distributions are not Gaussian, error of the mean is not simply related to variance. Error for a distribution of N dwell times is calculated by creating 200 bootstrap distributions of size N from the data set. The mean values of these distributions form a Gaussian, and the standard deviation of the Gaussian is the error of the mean dwell. The N for each condition is presented in Supplemental Data online.

Equation 2 was fit to mean dwells at 2 mM ATP and 100 μM ATP using the method of least squares (solid lines), yielding $\tau_b = 0.30 \pm 0.01$ s, $\tau_m = 0.28 * 10^{-20} \pm 1.40 * 10^{-20}$ s, and $\delta = 91.2 \pm 9.9$ nm with R (correlation coefficient) = 0.996 for the former and $\tau_b = 0.16 \pm 0.09$ s, $\tau_m = 0.30 \pm 0.10$ s, and $\delta = 2.90 \pm 1.68$ nm with R = 0.992 for the latter. Because 1 μM ADP has a negligible effect on stepping kinetics at zero load, Equation 2 was fit to the mean dwells taken in the presence of ADP with the added constraint $\tau_b + \tau_m = 0.3$ s (solid line). This ensures that the fit curve for 2 mM ATP and the fit curve for 1.5 mM ATP and 1 μM ADP meet at zero load while reducing the number of fit parameters. The fit yielded $\tau_b = 0.26 \pm 0.04$ s (and thus $\tau_m = 0.04$ s) and $\delta = 6.33 \pm 2.51$ nm with R = 0.974. Fits were done in Kaleidagraph (Synergy Software, Reading, Pennsylvania).

(B) Time trace of the detection bead position for the dual optical trap assay without feedback, performed at 1.5 mM ATP and 100 μM ADP. At 7 s, the bead is translocated due to binding of myosin VI. At 18 s, the myosin releases the actin dumbbell. The thick line is the averaged bead position.

Thus, we hypothesize that the myosin VI stepping cycle consists of a single, strongly load-dependent transition, but load does not affect the kinetics of motor stepping until high forces because biochemistry dominates the chemomechanical cycle.

At Saturating ATP, Dwell Time Distributions Fit Well to a Stepping Model Involving Two Irreversible Rates

By observing the individual steps of a myosin, a distribution of dwell times is gathered. While averaging these

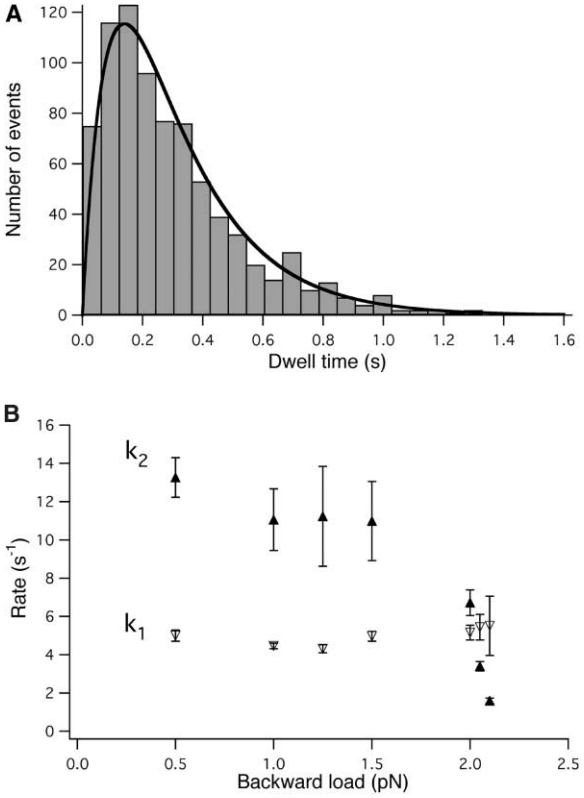

Figure 3. Kinetic Modeling of Dwell Distributions at Saturating ATP

(A) Histogram of dwell times for stepping against 1 pN load at saturating ATP (N = 991, 30 bins). The line is a fit of Equation 3 to the histogram, yielding $k_2 = 10.8 \pm 1.8\ s^{-1}$ and $k_1 = 4.46 \pm 0.19\ s^{-1}$. Fitting is done using maximum-likelihood algorithms developed in Matlab (Mathworks), and errors are the diagonal elements of the likelihood functions's covariance matrix. The goodness of the fit is tested with a χ^2 test comparing the dwell distribution predicted by Equation 3 with the empirical histogram. The two are not statistically distinguishable (p = 0.4137, N = 30).

(B) k_1 (▽) and k_2 (▲) as functions of load for stepping at 2 mM ATP. The fit values and errors are determined as described above. The goodness of each fit is tested with a χ^2 test as described above. The fit models are not statistically distinguishable from experimental results (p = 0.350, 0.228, 0.456, 0.317, 0.916, 0.268 for Load = 1, 1.25, 1.5, 2, 2.05, 2.1 pN, respectively; N = 30 for each).

dwells reveals information about the mean catalytic rate of the motor, the raw dwell distribution reveals more detailed information about individual transitions within the catalytic cycle.

The dwell distribution in Figure 3A fits well to a model approximating the motor's cycle by two irreversible steps (Figure 3A legend). The dwell distribution predicted by such a model is given by:

$$P(t;k_1,k_2) = \frac{k_1 k_2}{k_1 - k_2} \times \{\exp(-k_2 t) - \exp(-k_1 t)\} \quad (3)$$

where $P(t;k_1,k_2)dt$ is the normalized probability for a dwell time with duration between t and $t + dt$ given the rates k_1 and k_2.

This equation was fit to dwell distributions collected at saturating ATP and various loads, and the fit rate constants are plotted as functions of load in Figure 3B. Using these data, we model the kinetics of the myosin VI stepping cycle by two irreversible rates, one of which is affected by load. We denote k_1 as the load-independent rate and k_2 as a rate that decreases with increasing load. k_1 is the slower of the rates at loads up to 2 pN and remains constant at $\sim$5 s^{-1}. k_2 is $\sim$11 s^{-1} at low loads and decreases with increasing force until, at 2 pN, it becomes the slower of the two rates.

k_1 Is the Rate of ADP Release from the Trailing Myosin VI Head, and k_2 Describes a Combination of the Other Rates in the Stepping Cycle

From bulk biochemical studies of myosin VI, at saturating ATP, the slowest transition in the unloaded motor's stepping is hypothesized to be ADP release from the trailing head, represented by k_{+1} in Equation 1 (De La Cruz et al., 2001). From our approximate kinetic scheme in which the stepping cycle is reduced to two irreversible rates, k_1 corresponds to the slowest rate in the unloaded cycle, and our observed values for k_1 (Figure 3B) are consistent with the measured rate of ADP release of $\sim$5.5 s^{-1} determined by bulk assays (De La Cruz et al., 2001). k_1 thus appears to describe this ADP release rate.

From the fit of Equation 2 to the mean dwell data at saturating ATP (Figure 2A), we also observed that at loads below stall, the motor spends most of its stepping cycle undergoing biochemical transitions. This suggests that ADP release is not associated with the mechanical transition in the stepping pathway, consistent with our observation that k_1 remains constant over all loads.

The rate k_2 corresponds to a combination of the other rates in the stepping pathway. As described in the Experimental Procedures, at low loads, the value for k_2 is a lower limit to this combined rate. Within this rate is information about a rapid mechanical step, and at sufficiently high loads, k_2 describes the slowed rate for this transition.

This simplified stepping cycle can be represented by the following kinetic model, derived from Equation 1:

$$A \bullet MD \xrightarrow{k_1} A \bullet M \xrightarrow[\leftrightarrow MT \leftrightarrow MDP_i \leftrightarrow]{k_2(F)} A \bullet MD. \quad (4)$$

k_1 describes ADP release from the actin bound myosin head while $k_2(F)$ describes a combination of the other transitions in the stepping cycle, one of which displays a dependence on backward load F.

By Reducing ATP Concentration, ATP Binding to the Trailing Myosin VI Head Is Made the Slowest Transition in the Stepping Cycle

Mean dwell was measured at 1 pN of load while varying ATP from 70 μM to 2 mM (Figure 4A). At concentrations less than 1 mM, mean dwell increases as ATP is lowered, suggesting that binding of ATP to the trailing myosin VI head (represented by $[ATP]k_{+2}$ in Equation 1) is becoming so slow that it dominates the overall rate of stepping.

We confirm this by fitting Equation 3 to our experimental dwell time distributions. According to the kinetic model in Equation 4, the fit to dwell distributions collected at 1 pN load and varying ATP concentration should yield one rate corresponding to ADP release from the trailing myosin VI head (k_1 in Equation 4) and a sec-

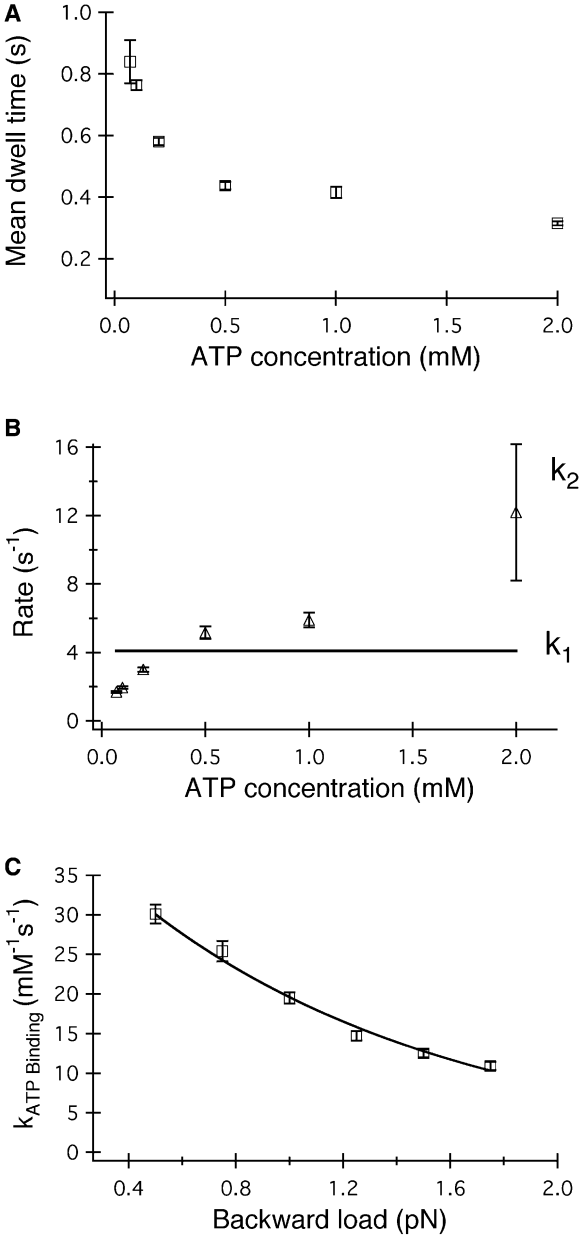

Figure 4. Effect of ATP on Myosin VI Stepping

(A) Mean dwell as a function of ATP concentration at 1 pN load. Errors are determined as described in the Figure 2A legend.

(B) Values for k_1 and k_2 when Equation 3 is simultaneously fit to dwell distributions collected at 1 pN of load and ATP concentrations ranging from 70 μM to 2 mM. k_1 is constrained to be identical for all distributions, and k_2 is allowed to vary. The fit values and errors are determined as described in the Figure 3A legend. A χ^2 test was used to compare the fit relations to the empirical histograms. The two are not distinguishable for most conditions ($p = 0.325, 0.084, 0.027, 0.827, 0.166, 0.894$ for ATP = 2, 1, 0.5, 0.2, 0.1, 0.07 mM, respectively; $N = 30$ for each).

(C) The rate of ATP binding as a function of load. These rates are determined from fits of Equation 3 to dwell distributions collected at 100 μM ATP and varying load, as described in the Results. The fit values and their errors are determined as described in the Figure 3A legend. A χ^2 test was used to compare the fit relations to empirical histograms. The two are not distinguishable for most conditions ($p = 0.104, 0.079, 0.166, 0.173, 0.376, 0.017$ for Load = 0.5, 0.75, 1, 1.25, 1.5, 1.75 pN, respectively; $N = 30$ for each).

The solid line is a fit of the ATP binding rates to Equation 5 with resulting values of $k_{ATP\ binding}(0) = 0.047 \pm 0.020\ \mu M^{-1}s^{-1}$ and $\delta = 3.5 \pm 1.9$ nm with R (correlation coefficient) = 0.991. The fit was done by the method of least squares using Kaleidagraph (Synergy Software, Reading, Pennsylvania).

ond rate which decreases as ATP concentration is lowered (k_2 in Equation 4). At high ATP concentrations, the latter rate corresponds to a combination of rates, and at low ATP concentrations, this rate is dominated by the slowed ATP binding rate.

Equation 3 was simultaneously fit to dwell distributions collected at 1 pN load and six different ATP conditions, and one of the two rates was constrained to be identical for all distributions. This anticipated model fits the data well (Figure 4B legend), and the constrained rate common to all the distributions is 4.1 s^{-1}, similar to the ADP release rate measured earlier. The second fit rate decreases as ATP is lowered (Figure 4B), and at 200 μM ATP and lower, this rate, presumably dominated by ATP binding, is the slowest transition in the stepping cycle.

At Low ATP Concentrations, Step Size Is Not Strongly Affected by Load and Kinetic Activity Slows with Load

Lowering ATP concentration to 100 μM, a concentration at which the slowest step in the myosin VI catalytic cycle is ATP binding, has little effect on forward and backward step size as a function of load (Figure 1). The dependence of mean dwell on load is strikingly changed, however, and at this low ATP concentration, mean dwell increases significantly as load is increased (Figure 2A).

ATP Binding Is Associated with a Mechanical Transition and Slows with Increasing Load

To interpret the load-dependent kinetics at 100 μM ATP, the mean dwell data are fit to Equation 2 (Figure 2A). The resulting fit yields $\tau_b/(\tau_b + \tau_m) = 0.4$ and $\tau_m/(\tau_b + \tau_m) = 0.6$, indicating that the motor is spending a greater amount of its chemomechanical cycle undergoing mechanical transitions. Because the motor spends most of its cycle waiting for ATP to bind to the rear head, this binding event appears to be associated with a mechanical step.

The fit value of δ, denoted δ_2, is ~3 nm, suggesting that this mechanical transition is unique from the more load-sensitive transition described by δ_1. This load-affected transition is presumably not apparent in the earlier data because, at 2 mM ATP, the rate of ATP binding is very rapid. Thus, at saturating ATP, the observed kinetics is dominated by the load-insensitive ADP release rate over most loads, obscuring effects of load on ATP binding.

The dwell distributions collected at 100 μM ATP and varying load were fit to the model represented by Equation 3. One of the fit rates should correspond to ATP binding, the slowest step in the kinetic cycle, while the other should correspond to ADP binding, which is the next slowest step and which we know is much slower than other rates in the stepping cycle. Equation 3, with one rate constrained to 4.1 s^{-1} (the ADP release rate in Figure 4B), was fit to each dwell distribution, yielding

the apparent rate of ATP binding as a function of load. Dividing these rates by 100 μM yields values for the second order ATP binding rate (Figure 4C).

According to the energy landscape picture of load-affected kinetics, a mechanical rate obeys the relation

$$k = k(0) \times \exp\left(-\frac{F\delta}{k_B T}\right) \quad (5)$$

where $k(0)$ is the unloaded rate and δ is the distance to the transition state of the mechanical step (Wang et al., 1998). The calculated ATP binding rates were fit to this relation (Figure 4C), yielding a zero-load rate of 0.05 $\mu M^{-1}s^{-1}$, somewhat higher than the rate of 0.02 $\mu M^{-1}s^{-1}$ measured in bulk myosin VI assays (De La Cruz et al., 2001). The fit value of δ is 4 nm, similar to the measured value for δ_2, as expected.

In the Presence of ADP, Myosin VI Stepping Is Inhibited in a Load-Dependent Manner

To observe effects of ADP on myosin VI stepping, the gliding filament assay (see Experimental Procedures) was used to measure the amount of ADP necessary to inhibit actin motility at near-zero load and an ATP concentration that is saturating in the absence of ADP (1.4 mM) (Figure 5A). At near-zero loads, gliding filament velocity was not significantly slowed until relatively high concentrations of ADP. Two-fold inhibition is observed in the presence of 400 μM ADP.

The dual optical trap assay was then used to observe effects of ADP on the mean dwell of myosin VI stepping against load. With a backward load of 1 pN, dramatic slowing of stepping occurs at much lower ADP concentrations than in the gliding filament assay (Figure 5B). At only 2 μM ADP, the mean dwell of the motor increases about 1.5-fold. According to the gliding filament data, this amount of ADP coupled with near-zero load has almost no effect on the kinetics of motor stepping.

At High ATP Concentration and in the Presence of ADP, Step Size Is Not Strongly Affected by Load and Kinetic Activity Slows with Increasing Load

To examine this correlation between ADP and load effects, step size and dwell time data were collected at 1.5 mM ATP, 1 μM ADP, and varying load. The dependence of step size on load is not affected by ADP (Figure 1). The effect of load on mean dwell, however, is strongly affected by ADP (Figure 2A). Dwell increases with increasing load at lower forces than was observed in the absence of ADP.

ADP Binding Is Associated with a Mechanical Transition and Increases with Increasing Load

Again considering the Boltzmann model represented by Equation 2, in the presence of ADP, $\tau_m/(\tau_b + \tau_m)$ is significantly increased from its value in the absence of ADP, indicating that mechanical transitions dominate more of the chemomechanical cycle. Also, mean dwell increases less rapidly with load due to a smaller δ, denoted δ_3, of 6 nm (Figure 2A). Thus, the load-affected kinetics results from a mechanical transition that is

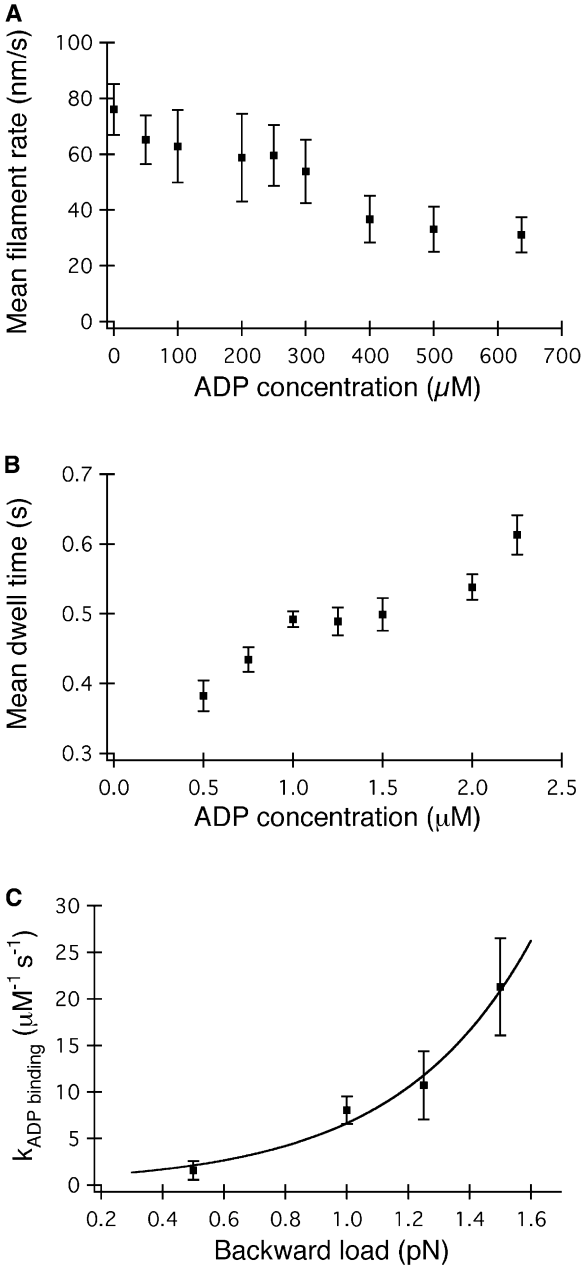

Figure 5. Effect of ADP on Myosin VI Stepping

(A) Actin gliding filament velocity as a function of ADP concentration at 1.4 mM ATP. Each data point is the mean of 10 measured velocities, and the error is the standard deviation.

(B) Mean dwell as a function of ADP concentration at 1.5 mM ATP and 1 pN backward load. Errors were calculated as described in the Figure 2A legend.

(C) The rate of ADP binding as a function of load. These rates are derived using Equation 7 as described in the Results. Errors are determined by propagating the errors on $k_1(F)$, $k_2(F)$, and $\bar{\tau}(F,[ADP] = 1\mu M)$. The solid line is a fit of the ADP binding rates to Equation 5 with the resulting values of $k_{ADP\ binding}(0) = 0.67 \pm 0.29\ \mu M^{-1}s^{-1}$ and $\delta = -9.2 \pm 1.2$ nm with R (correlation coefficient) = 0.993. The fit was done by the method of least squares using Kaleidagraph (Synergy Software).

unique from and less load sensitive than the mechanical transition described by δ_1.

A possible explanation for these results is that the rate of ADP binding to the trailing myosin VI head increases with load. According to this model, pulling back on the motor increases the rate of ADP binding to the rear head and thus prevents ATP from binding. This prevents the head from dissociating from actin and so slows stepping. Because, in the absence of ADP, the apparent rate of ADP binding is zero, we do not see this load effect in our kinetics at saturating ATP in the absence of ADP.

To test this hypothesis, we consider the dependence of mean dwell time on ADP concentration. At high ATP concentrations and in the presence of ADP, we hypothesize that our kinetic scheme in Equation 4 should take the revised form:

$$A \bullet MD \underset{[ADP]k_{-1}(F)}{\overset{k_1}{\leftrightarrow}} A \bullet M \xrightarrow[\leftrightarrow MT \leftrightarrow MDP_i \leftrightarrow]{k_2(F)} A \bullet MD \quad (6)$$

where $k_{-1}(F)$ represents the second order rate of ADP binding, a load-dependent transition. Our observation that ADP release appears load independent while ADP binding is load dependent suggests that ADP release is an Eyring-like process, with a transition state similar to the initial state. Alternatively, our results may indicate that ADP release is a macroscopic transition incorporating more than one microscopic rate. This transition could include a load-dependent mechanical transition that is coupled to load-independent ADP association and dissociation. Such coupling could account for our observed load effects and is consistent with recent observations by E. De La Cruz that ADP binding to actin bound myosin VI occurs via a multistep mechanism (personal communication).

Using this kinetic model, we calculate the dependence of mean dwell on the three rates to be:

$$\frac{1}{\bar{\tau}(F,[ADP])} = \frac{k_1 k_2}{[ADP]k_{-1} + k_1 + k_2}. \quad (7)$$

According to this relation, mean dwell is linearly related to ADP concentration at a given load, consistent with our data in Figure 5B.

We further test this model by using the derived values for k_1 and $k_2(F)$ (Figure 3B) along with mean dwells measured at 1 μM ADP and varying load, $\bar{\tau}(F,[ADP] = 1\mu M)$ (Figure 2A), to calculate the rate of ADP binding as a function of load, $k_{-1}(F)$, using Equation 7. These calculated values are shown in Figure 5C. We then compared our experimental dwell distributions at 1.5 mM ATP, 1 μM ADP, and varying load to the distributions predicted by the three derived rates $k_1(F)$, $k_2(F)$, and $k_{-1}(F)$. The predicted distributions match well with empirical results (see Supplemental Data at http://www.cell.com/cgi/content/full/116/5/737/DC1), and so the model appropriately describes load effects in the presence of ADP and at high ATP concentrations.

We fit the calculated values of $k_{-1}(F)$ to Equation 5 (Figure 5C), yielding an unloaded rate of ADP binding of 0.67 $\mu M^{-1}s^{-1}$ and a δ of -9 nm (slightly larger in magnitude than δ_3). δ is negative so that Equation 5 describes a rate that increases with increasing load.

Our Results at Varying ATP, ADP, and Load Conditions Suggest an Approximate Kinetic Scheme Involving Two Mechanical Transitions

Combining our results at varying ATP and ADP concentrations into our stepping model, we arrive at the following kinetic scheme:

$$A \bullet MD \underset{[ADP]k_{-1}(F)}{\overset{k_1}{\leftrightarrow}} A \bullet M \xrightarrow{[ATP]k_2(F)} MT \xrightarrow[\leftrightarrow MDP_i \leftrightarrow]{k_3(F)} A \bullet MD. \quad (8)$$

k_1 again represents a load-independent ADP release rate. $k_{-1}(F)$ and $k_2(F)$ describe the rates of ADP and ATP binding, respectively, both of which are affected by backward load, F. $k_3(F)$ is a combination of other rates in the stepping cycle, and within this rate is information about a strongly load-sensitive transition. At saturating ATP and in the absence of ADP, this scheme reduces to Equation 4.

Given the geometry of a myosin VI molecule, the 8 nm change in forward step with increasing load (Figure 1) may be due to strain deforming the trailing head of the motor, forcing the lead head to bind to an actin binding site one or two monomers short of its unloaded binding site. The values for δ_2 of 3 nm and δ_3 of 6 nm are consistent with this deformation affecting the ADP and ATP binding of the trailing head. We thus speculate that backward load strains and "pulls back" the motor, resulting in the observed effects on step size and kinetics.

At Physiological Nucleotide Conditions, Myosin VI Stepping Is Inhibited at Sub-PicoNewton Loads

In many cells, the ADP concentration is maintained on the order of 100 μM while ATP is maintained around 1–5 mM (Mathews and Van Holde, 1996; Roth and Weiner, 1991; Stryer, 1995). According to the model in Equation 8 and our empirically derived rates, inhibition of stepping at physiological conditions may occur at loads that are considerably lower than the stall forces measured at saturating ATP. To test this, we performed our trap assays at 100 μM ADP and 1.5 mM ATP. Under these conditions, we found that the motor dwells for extremely prolonged periods of time immediately after binding to actin, preventing us from implementing our optical trap feedback (Figure 2B). This result suggests that the backward load developed when a motor takes a single step against the trap is enough to stall its kinetics.

Our trap stiffness is about 0.01 pN/nm, and so a 30 nm step develops about 0.3 pN of load. From our fit of the ADP binding rate data to Equation 5 (Figure 5C), at these nucleotide concentrations and load, the rate of ADP binding is $\sim$130 s^{-1}. If we also assume that, in the presence of 1.5 mM ATP and at sub-pN loads, our kinetic cycle is represented by Equation 6 with $k_1 \sim$4.5 s^{-1} and $k_2(F) \sim$11 s^{-1}, then Equation 7 predicts a mean dwell of 3 s. Dwells of this length and longer were observed. Figure 2B is an example of a motor that is bound to the actin filament for 11 s before releasing.

Discussion

A Simple Stepping Model Involves a Flexible N-Terminal Portion of the Myosin VI Tail

We hypothesize that some part of myosin VI must be flexible and extended to account for the large diffusive steps of the motor. Stepping could then occur through a working stroke of ~10 nm followed by an ~20 nm diffusive search of the actin-dissociated myosin VI head.

Though the location of such a flexible region is not known, we conjecture that the first ~70 residues of the tail domain, just beyond the second calmodulin binding site of the lever arm, are likely to be involved. Using the Paircoil program (Berger et al., 1995), we assayed the tail sequences of eight myosin VI variants from seven different organisms for their proclivity to form a coiled-coil structure (data not shown). In all cases, the propensity of the first ~70 residues of the tail to form a coiled-coil is very low, with the *Drosophila* myosin VI showing almost no propensity at all. This suggests that the N-terminal ~70 residues of the tail just adjacent to the light chain binding domains (which we refer to as the *N-terminal tail domain*) remain in a relatively unstructured conformation and thus may constitute the putative flexible region. This idea is further supported by our observations that this region of the tail is highly susceptible to proteolysis, indicating that these residues may be relatively unstructured (B. Rami and B. Spink, personal communication).

If the N-terminal tail domain is flexible, then the step size of the motor should be dictated by the length of its working stroke and the length of the N-terminal tail domain for each of its two heavy chains. A sequence of 70 amino acids is ~27 nm fully extended, but in an unstructured state, the most likely conformation is a compact structure with end-to-end distance of ~6.5 nm (see Supplemental Data on *Cell* website). Thus, the two N-terminal tail domains of the myosin VI homodimer may contribute to the observed 12 nm working stroke an additional ~13 nm reach, yielding a possible step size of ~25 nm. This step size nearly accounts for the mean step of the motor, and a longer step could result from elongated configurations of the flexible tail regions as they explore their conformational spaces.

However, we conjectured in the Results that an applied load of 2 pN can deform the actin bound trailing head, suggesting that we are pulling on a rigid element adjoined to this head. This suggests that load may prevent the N-terminal tail domain of the trailing actin bound head from contributing to the forward reach, making it harder to reconcile large observed steps with the motor's geometry. Furthermore, because the duration of a diffusive search is sensitive to load (Howard, 2001), a stepping mechanism with both N-terminal tail domains remaining flexible may not be consistent with our observation that the motor's step size and mean dwell are insensitive to loads up to 2 pN. Estimating the time for a myosin VI head to diffuse against an external force (see Supplemental Data online), we found that, for a motor stepping against 2 pN of load, the dwell time should be considerably longer than the unloaded dwell for steps greater than 35 nm due to slowing of the diffusive search. At 2 pN load, however, we observe myosin VI steps that are upwards of 40 nm, yet the motor's mean dwell time is unaffected by this load.

A Modified Stepping Model Predicts that the Beginning of the Tail Changes between Rigid and Flexible Conformations

We suggest a modification of the above stepping model to account for the insensitivity of the motor's step size and mean dwell time to loads. We propose that, while the actin-dissociated lead head is at the end of a flexible and elongated region of the motor, the actin bound trailing head is maintained in a rigid conformation that bears the external force and so shields the free head from load. In this way, the actin-dissociated head is able to undergo an unloaded diffusive search for its actin binding site even when an external load is applied against the motor's stepping. Again, we hypothesize that the N-terminal tail domain is involved in this mechanism. This region may adopt a rigid structure when the myosin VI head is bound to actin, either by folding itself into a compact and rigid form or by docking to another part of the motor or to the actin. When the head dissociates from actin, the N-terminal tail domain then adopts its flexible and relatively unstructured conformation, allowing for the diffusive search.

A cartoon representation of a putative myosin VI stepping mechanism is shown in the *Unloaded Stepping* model in Figure 6. This representation describes the second of the two proposed stepping models and thus shows the N-terminal tail domain alternating between rigid and flexible conformations. The simple stepping model, described in the first section of the Discussion, is identical to this representation, except both N-terminal tail domains remain flexible and elongated throughout stepping.

We consider the cycle starting from state (A): one head is bound to actin and has ADP in its nucleotide binding pocket while the other head is free from actin and has a bound ATP. Before the free head binds actin, its N-terminal tail domain must adopt a flexible conformation. This flexible configuration is represented by a thin curved line, and in our model, this transition from a rigid to a flexible state coincides with ATP hydrolysis. More generally, we predict this transition must occur sometime after the free head is released from actin and before it releases its phosphate and is strongly bound to actin again. The N-terminal tail domain of the actin bound myosin head with bound ADP, on the other hand, is in a rigid conformation. We predict it is either folded into a compact form or docked to another part of the motor or the actin (not shown), and its rigidity helps shield the actin-dissociated head from load.

The actin-dissociated head hydrolyzes its ATP (B) and finds its next actin binding site through a diffusive search at the end of its N-terminal tail domain. Upon binding actin (C), this head has become the lead head, and it releases its phosphate (D). The motor spends most of its time in this state, waiting for the trailing head to release its ADP.

As already discussed, the N-terminal tail domain of an actin bound myosin head with bound ADP is predicted to be rigid. We thus hypothesize that the N-terminal tail domain associated with the lead head in (D) attempts

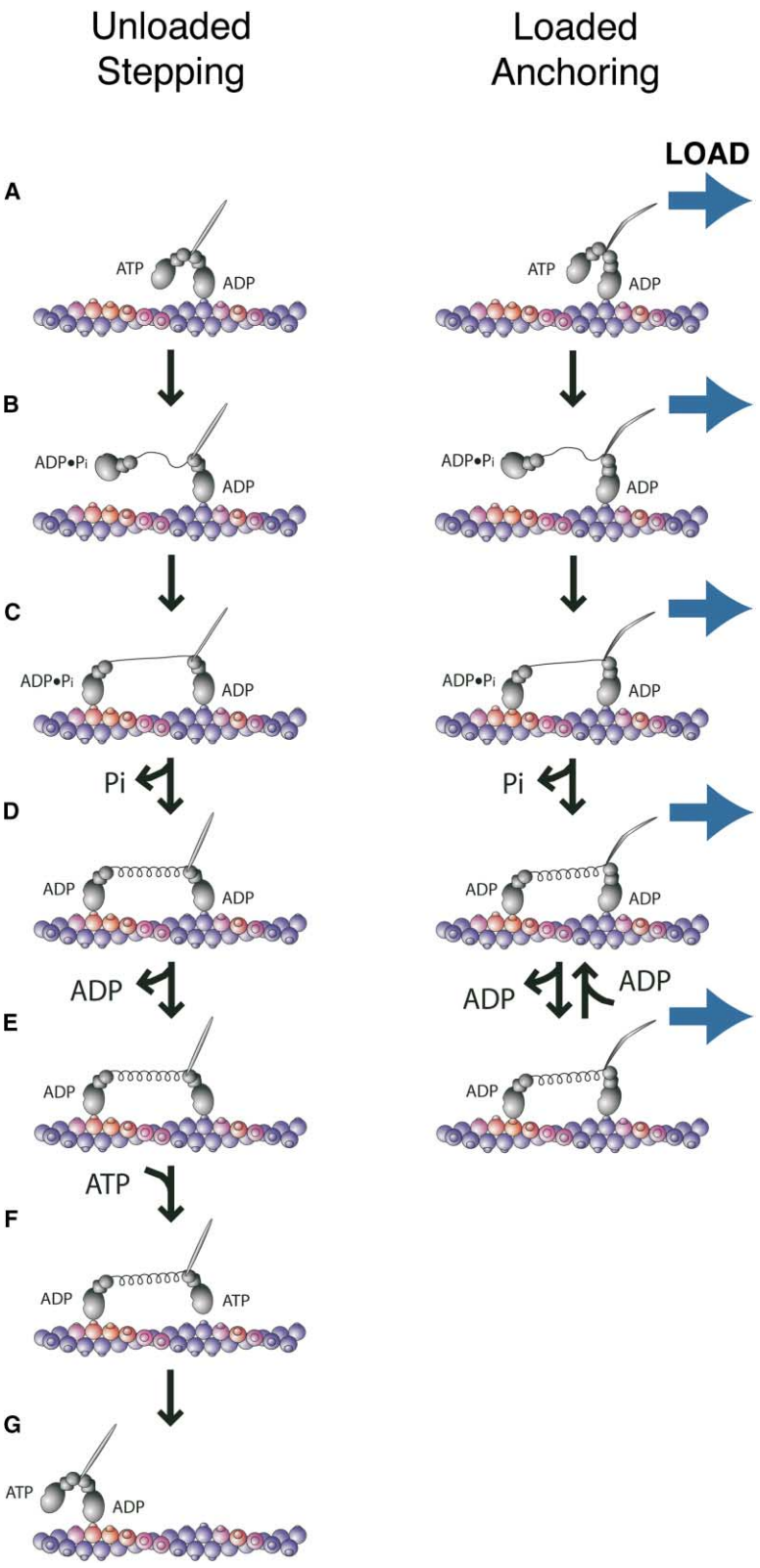

Figure 6. Model for Myosin VI Stepping and Anchoring

The stepping and anchoring models are described in the Discussion. The cartoon model shown here assumes that the first ~70 residues of the tail just adjacent to the light chain binding domains (referred to as the N-terminal tail domain) alternate between a rigid and flexible conformation depending on the state of the catalytic head. A simpler model, presented in the first section of the Discussion, is identical to the cartoon model shown here except that the N-terminal tail domain does not transition to a rigid form and instead remains extended and flexible throughout stepping.

Each myosin VI monomer within the homodimer is represented as an oval, describing the catalytic domain, a square, representing the ~50 residue insert unique to this myosin (Wells et al., 1999), and a circle, representing the light chain. The coiled-coil tail region joining the two heads is represented by a rod. When the N-terminal tail domain is flexible and extended, this region is represented by a thin line. When this domain is rigid, which is hypothesized to result either from the domain folding itself into a compact structure or from it docking to part of the motor or actin, it is not shown.

Knobs on the actin filament indicate stereospecific myosin binding sites. Actin subunits in red indicate preferred binding sites for the free myosin head according to observed stepping distributions (Rock et al., 2001). The spread of the color in adjacent actin monomers from red to blue reflects the spread in step size.

The *Unloaded Stepping* model is presented on the left side of the figure while the *Loaded Anchoring* model is presented on the right, as indicated. In the *Loaded Anchoring* model, the blue arrow represents backward load, and the rod representing the tail region is curved to indicate the strain induced by load. According to our model, when the motor behaves as an anchor, it remains predominantly in states (D) and (E) of the *Loaded Anchoring* model.

to transition back to its more rigid state. More generally, our model predicts that this transition from flexible to rigid must occur sometime between when this myosin head binds strongly to the actin and when it enters its ADP state. In (D), however, this transition cannot occur since both heads are tightly bound to the actin and are thus constrained across ~30 nm. The N-terminal tail domain cannot complete this transition until the rear

head releases from actin, and thus it is represented by a taut, stretched spring.

The rear head releases its ADP (E) and binds ATP, allowing it to release from actin (F). As the trailing head releases from the actin, the N-terminal tail domain of the lead myosin head is now able to become rigid (G). This transition from flexible to rigid causes the motor's center of mass to traverse its ~30 nm step, resulting in the large, rapid mechanical transition discussed in the Results. This process must generate sufficient force to drive motility by converting the free energy of this conformational change to mechanical work (Zhuang and Rief, 2003) and must be capable of occurring against up to 2 pN. Other such processes have been observed to produce forces from 2.5 to 25 pN (Kellermayer et al., 1997; Schwaiger et al., 2002). Thus, it is reasonable to envision that this putative transition drives motility of myosin VI against loads of up to 2 pN.

Load Causes Myosin VI to Function as an Anchor In Vivo due to an Increased Rate of ADP Binding to the Trailing Head

As discussed in the Introduction, myosin VI anchoring may be the result of applied backward load halting stepping kinetics while the motor remains strongly bound to actin. We have shown here that the rate of ADP dissociation from the trailing head of the motor is not affected by load while the rate of ATP association is slowed and the rate of ADP association is increased. From our data (Figures 4C and 5C), we find that at zero load, the rates of ATP and ADP binding are 0.047 $\mu M^{-1}s^{-1}$ and 0.67 $\mu M^{-1}s^{-1}$, respectively, while at 1 pN load, they are changed to 0.020 $\mu M^{-1}s^{-1}$ and 6.7 $\mu M^{-1}s^{-1}$.

Assuming a physiological ADP concentration of 100 μM and ATP concentration of 5 mM and using the rates above, under no load conditions, the in vivo ATP binding rate is 235 s^{-1} and the ADP binding rate is 67 s^{-1}, while at 1 pN of load, the ATP binding rate is 100 s^{-1} and the ADP binding rate is 670 s^{-1}. Thus, at physiological conditions, the predominant effect of backward load is a slowing of motor stepping due to an increase in the ADP binding rate, making ADP binding competitive with ATP binding. By such a mechanism, physiological ADP coupled with sufficient load can switch the function of myosin VI from transporting to anchoring, such as we observed in Figure 2B.

This mechanism for anchoring is shown in the *Loaded Anchoring* model in Figure 6. The motor goes through the same states (A)–(E) as in the *Unloaded Stepping* model. We hypothesize, however, that the applied backward load causes a deformation of the trailing head that results in a small decrease in the forward step size as well as a change in the stepping kinetics such that ADP binding is competitive with ATP binding. Thus, according to this model, a motor experiencing sufficient backward load is anchored to actin and remains predominantly in states (D) and (E) of the *Loaded Anchoring* model.

Our Model Accounts for Two Distinct Functions of Myosin VI

We now consider two hypothesized in vivo functions of myosin VI and attempt to explain how they occur from a mechanistic point of view. First is the motor's role in clathrin-mediated endocytosis in which it is thought to move vesicles to within a cell (Buss et al., 2001a). Assuming that a clathrin-coated vesicle is ~100 nm in diameter (Buss et al., 2001a) and that the viscosity within a cell is about 50 times that of water (Boal, 2002), we can calculate the backward load due to viscous drag as the motor moves the vesicle at ~80 nm/s. Approximating that the vesicle remains spherical, the motor experiences a backward load of 4 fN, orders of magnitude smaller than forces we have explored empirically. Using the rates derived in the Results, we find that this load causes the rate of ADP binding to increase by only 0.4% from its unloaded value. Thus, the motor is able to step processively against this load at physiological nucleotide concentrations, allowing it to transport endocytic cargo by the stepping mechanism discussed earlier.

A second hypothesized role of myosin VI is maintaining the structural integrity of stereocilia at the apical surface of inner ear hair cells. In myosin VI null mice, the apical surface is seen to lose position and rise up between the stereocilia (Cramer, 2000). Myosin VI may function by associating at its tail region with this apical membrane. Actin filaments within stereocilia are polarized, with their minus ends facing the roots where the stereocilia enter the hair cell, and so the myosin VI motor may walk toward the root and pull the membrane down between the stereocilia (Cramer, 2000). As the motor steps, an increasing force against its motion will develop once the apical surface is pulled taut. Eventually, this backward load, coupled with physiological nucleotide, will stall the motor's stepping, causing it to anchor the membrane between the stereocilia.

Experimental Procedures

Protein Constructs and Expression

Experiments described here utilize a double-headed myosin VI/GFP construct as described (De La Cruz et al., 2001). In brief, porcine myosin VI cDNA was truncated at Arg992 to include 20 native heptad repeats of coiled-coil. This was followed by a leucine zipper (GCN4) to ensure dimerization (Trybus et al., 1997) and then the cDNA for enhanced GFP (EGFP; BD Biosciences Clontech, Palo Alto, California). Finally, a Flag tag (encoding GDYKDDDDK) was included at the C terminus to facilitate purification (Sweeney et al., 1998).

This cDNA was used to generate a recombinant baculovirus that was used for coexpression of the myosin VI/GFP construct with calmodulin, the physiological light chain (Hasson and Mooseker, 1994), from chicken. Generation of recombinant baculovirus, expression in SF9 cells, and protein purification follow published procedures (De La Cruz et al., 2001; Sweeney et al., 1998).

Flow Cell Preparation

Optical trap and gliding filament assays were performed in flow cells prepared as described (Rock et al., 2000). For optical trap experiments in the absence of ADP, assay buffers include 25 mM imidazole HCl (pH 7.4), 25 mM KCl, 4.5 μM calmodulin, 1 mM EGTA, 10 mM DTT, 4 mM $MgCl_2$, an oxygen-scavenging system to retard photobleaching (25 μg/ml glucose oxidase, 45 μg/ml catalase, 30.8 mM β-mercaptoethanol, 0.5% glucose), and an ATP-regeneration system (0.1 mg/ml creatine phosphokinase, 1 mM creatine phosphate). Experiments at saturating ATP in the absence of ADP were conducted at 2 mM ATP.

Optical trap experiments in the presence of ADP used identical buffer conditions except that the ATP regeneration system was not included. Assays at high ATP in the presence of ADP were conducted at 1.5 mM ATP. In the gliding filament assay, kinetics of stepping is observed to be saturated at both 1.5 mM and 2 mM ATP in the absence of ADP (see Supplemental Data on *Cell* website).

Gliding filament assay buffer conditions were identical to the opti-

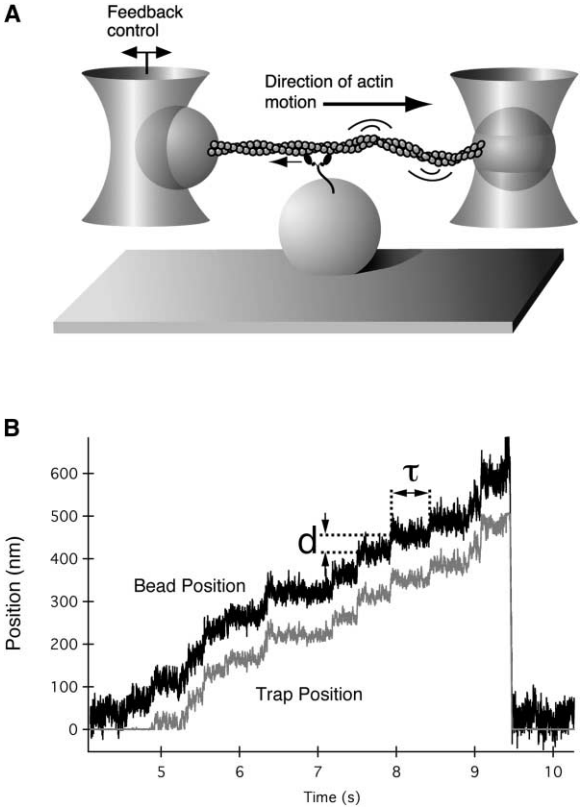

Figure 7. The Dual Optical Trap Assay

(A) Experimental geometry for the optical trap assay. An actin filament is attached to two polystyrene beads (represented by spheres) that are held in independently controlled optical traps (depicted as hourglass shapes) forming an actin "dumbbell." The dumbbell is brought into contact with myosin VI/GFP construct adsorbed to a motor platform on the surface through anti-GFP antibodies coating the surface. Feedback maintains a constant distance between the bead that is being pulled by the motor and the trap that holds this bead, ensuring constant load against stepping.

(B) Example data trace from the dual trap assay. The top, black time trace is the position of the dumbbell bead translocated by myosin VI. The lower, gray time trace is the position of the optical trap holding this bead. Once the myosin moves the bead out of the trap a sufficient distance, the trap follows the bead at a fixed distance to maintain constant load against stepping. Examples of the two tabulated observables, dwell time (τ) and step size (d), are highlighted. The data shown are stepping against 1 pN load at 2 mM ATP.

cal trap assays and also did not include ATP regeneration system. ATP concentration was 1.4 mM, which is saturating in the absence of ADP, and ADP concentration varied from 0 to 640 μM.

To attach myosin VI to the surface of the flow cell, the surface was sparsely covered with 1.5 μm diameter glass beads, which act as motor "platforms." This surface was then coated with nitrocellulose. 0.05 mg/ml mouse monoclonal anti-GFP antibody (mAB 3E6, Q-Biogene, Carlsbad, California) was flowed into the cell followed by 1 mg/ml BSA to block the nitrocellulose surface. Dilute motor was flowed into the cell and attached to the surface via binding between anti-GFP antibody on the surface and GFP on the motor's C-terminal end.

Purification of Nucleotides

Because ATP stocks can contain 1% or more ADP contamination, we purified ATP that was used in assays without an ATP-regeneration system by liquid chromatography. An ÄKTA FPLC system (Amersham Biosciences, Piscataway, New Jersey) was used with an anion-exchange column (MonoQ HR 5/5, Amersham Biosciences). Nucleotide was loaded on the column with 25 mM imidazole HCl, 4 mM $MgCl_2$ (pH 7) and eluted with a 0%–55% gradient of 25 mM imidazole HCl, 4 mM $MgCl_2$, 500 mM KCl (pH 7). ADP was purified identically.

Optical Trap Assay

Dual optical trap experiments were performed as described (Rock et al., 2000, 2001). Experiments were conducted at ~22°C. Briefly, two neutravidin-coated polystyrene beads, 1 μm in diameter, are held in two independently controlled laser traps. A phalloidin-stabilized actin filament that has been biotinylated is attached to the beads through biotin-neutravidin linkages, forming an actin "dumbbell" (Figure 7A).

The dumbbell is brought near a 1.5 μm diameter glass bead platform on the myosin-coated surface. As a myosin on the platform translocates the actin, one of the beads, the "feedback bead," is pulled out of its trap. We observe a motor's stepping through detection of the feedback bead's position. A constant force is maintained against stepping by using a feedback system to control the position of the trap holding the feedback bead. As the bead is moved out of the trap, the trap follows at a fixed distance, ensuring that every step is taken against the same load. Because an optical trap behaves like a linear spring potential (Dai and Sheetz, 1995), we can measure the spring constant describing the trap's stiffness (Sheetz, 1998). Using this measurement, a fixed distance between the trap and bead is converted to a known backward load.

For this assay, data collected are time traces of the feedback bead position (Figure 7B). These traces show the bead alternating between a dwelling state, in which the motor is not moving the actin, and a rapid mechanical transition during which translocation of actin occurs. The two observables tabulated from this data are dwell time (τ) and step size (d). d is the distance between successive dwells, and τ is the time between successive steps. Data are tabulated by hand using algorithms developed in Matlab (Mathworks, Natick, Massachusetts).

Because data are tabulated by hand, we are likely missing dwells occurring at very rapid time scales. The error due to these missed events must be considered when fitting Equation 3 to empirical dwell histograms (Figure 3A). The rapid rise in observed dwells at low times predominantly determines the fit value for the more rapid of the two rates, and the decrease in observed dwells at higher times describes the slower rate. Because of missed events at low times, the more rapid rate, if very fast, may be underestimated by our fit value. Thus, at saturating ATP, the calculated rate of ~11 s^{-1} for k_2 at low loads (Figure 3B) probably describes a lower limit to the actual rate, a limit that is dictated by the limitations of our analysis. Within this rate is information about a rapid mechanical transition that is slowed significantly at high loads. At these loads, k_2 decreases below this 11 s^{-1} lower limit and can be resolved by our fit to the dwell distribution.

To ensure that observed time traces result from individual motors and are not the result of more than one molecule translocating an actin, for a given flow cell, numerous surface platforms are tested for motor activity. Assuming a Poisson distribution describes the number of motors on a platform, when motor activity is observed on 10% of a flow cell's platforms, ~95% of the active platforms contain only a single motor (Block et al., 1990). Thus, only cells with motor activity on 10% or less of the surface platforms were used.

Data collected at identical nucleotide and load conditions but at different motors have been pooled together. To justify this, we have compared data collected at identical experimental conditions but different motors and found that dwell distributions from different motors are in general indistinguishable (see Supplemental Data on *Cell* website). The number of dwells and steps collected at each experimental condition are presented as Supplemental Data online.

For most experimental conditions (a given load and ADP and ATP concentration), data were collected from two to five motors. The number of motors is also listed in Supplemental Data.

Gliding Filament Assay

Gliding filament assays were performed as described (Rock et al., 2000). Temperature was maintained at 25°C. In brief, myosin VI is sparsely coated on the surface as described above. Actin filaments

labeled with and stabilized by tetramethyl rhodamine isothiocyanate (TRITC) phalloidin (Molecular Probes, Eugene, Oregon) are flowed into the cell. Images of the labeled actin being translocated by motor are captured and analyzed using the NIH Image software package (National Institutes of Health, Bethesda, Maryland). To ensure actin motility results from only a single myosin molecule, the assay is performed at dilute motor conditions where the translocated actin is observed to swivel about and move through a single point surface attachment.

Acknowledgments

We thank the Spudich and Block labs for invaluable discussion and R. Rock and E. Abbondanzieri for contributions to interpretation of results. We also thank B. Spink for help with statistical analysis, A. Meyer for help with purification of nucleotides, S. Bennett and the Brutlag lab for allowing us use of their computers, and T. Purcell for cover design. This work was supported by NIH Grant GM33289.

Received: August 13, 2003
Revised: November 25, 2003
Accepted: January 14, 2004
Published: March 4, 2004

References

Bahloul, A., Chevreux, G., Wells, A.L., Martin, D., Nolt, J., Yang, Z., Chen, L.-Q., Potier, N., Van Dorsselaer, A., Rosenfeld, S., et al. (2004). The unique insert in myosin VI is a structural calcium-calmodulin binding site. Proc. Natl. Acad. Sci. USA, in press.

Berger, B., Wilson, D.B., Wolf, E., Tonchev, T., Milla, M., and Kim, P.S. (1995). Predicting coiled coils by use of pairwise residue correlations. Proc. Natl. Acad. Sci. USA *92*, 8259–8263.

Block, S.M., Goldstein, L.S., and Schnapp, B.J. (1990). Bead movement by single kinesin molecules studied with optical tweezers. Nature *348*, 348–352.

Block, S.M., Asbury, C.L., Shaevitz, J.W., and Lang, M.J. (2003). Probing the kinesin reaction cycle with a 2D optical force clamp. Proc. Natl. Acad. Sci. USA *100*, 2351–2356.

Boal, D.H. (2002). Mechanics of the Cell (Cambridge: Cambridge University Press).

Buss, F., Arden, S.D., Lindsay, M., Luzio, J.P., and Kendrick-Jones, J. (2001a). Myosin VI isoform localized to clathrin-coated vesicles with a role in clathrin-mediated endocytosis. EMBO J. *20*, 3676–3684.

Buss, F., Luzio, J.P., and Kendrick-Jones, J. (2001b). Myosin VI, a new force in clathrin mediated endocytosis. FEBS Lett. *508*, 295–299.

Buss, F., Luzio, J.P., and Kendrick-Jones, J. (2002). Myosin VI, an actin motor for membrane traffic and cell migration. Traffic *3*, 851–858.

Cramer, L.P. (2000). Myosin VI: roles for a minus end-directed actin motor in cells. J. Cell Biol. *150*, F121–F126.

Dai, J., and Sheetz, M.P. (1995). Mechanical properties of neuronal growth cone membranes studied by tether formation with laser optical tweezers. Biophys. J. *68*, 988–996.

De La Cruz, E.M., Ostap, E.M., and Sweeney, H.L. (2001). Kinetic mechanism and regulation of myosin VI. J. Biol. Chem. *276*, 32373–32381.

Fabrizio, J.J., Hime, G., Lemmon, S.K., and Bazinet, C. (1998). Genetic dissection of sperm individualization in Drosophila melanogaster. Development *125*, 1833–1843.

Finer, J.T., Simmons, R.M., and Spudich, J.A. (1994). Single myosin molecule mechanics: piconewton forces and nanometre steps. Nature *368*, 113–119.

Fisher, M.E., and Kolomeisky, A.B. (1999). The force exerted by a molecular motor. Proc. Natl. Acad. Sci. USA *96*, 6597–6602.

Hasson, T., and Mooseker, M.S. (1994). Porcine myosin-VI: characterization of a new mammalian unconventional myosin. J. Cell Biol. *127*, 425–440.

Hasson, T., Gillespie, P.G., Garcia, J.A., MacDonald, R.B., Zhao, Y., Yee, A.G., Mooseker, M.S., and Corey, D.P. (1997). Unconventional myosins in inner-ear sensory epithelia. J. Cell Biol. *137*, 1287–1307.

Howard, J. (2001). Mechanics of Motor Proteins and the Cytoskeleton (Sunderland, MA: Sinauer Associates, Inc.).

Ishijima, A., Harada, Y., Kojima, H., Funatsu, T., Higuchi, H., and Yanagida, T. (1994). Single-molecule analysis of the actomyosin motor using nano-manipulation. Biochem. Biophys. Res. Commun. *199*, 1057–1063.

Kellermayer, M.S., Smith, S.B., Granzier, H.L., and Bustamante, C. (1997). Folding-unfolding transitions in single titin molecules characterized with laser tweezers. Science *276*, 1112–1116.

Mathews, C.K., and Van Holde, K.E. (1996). Biochemistry, 2nd edn. (Menlo Park: The Benjamin/Cummings Publiching Company, Inc.).

Mehta, A.D., Rock, R.S., Rief, M., Spudich, J.A., Mooseker, M.S., and Cheney, R.E. (1999). Myosin-V is a processive actin-based motor. Nature *400*, 590–593.

Nishikawa, S., Homma, K., Komori, Y., Iwaki, M., Wazawa, T., Hikikoshi Iwane, A., Saito, J., Ikebe, R., Katayama, E., Yanagida, T., and Ikebe, M. (2002). Class VI myosin moves processively along actin filaments backward with large steps. Biochem. Biophys. Res. Commun. *290*, 311–317.

Purcell, T.J., Morris, C., Spudich, J.A., and Sweeney, H.L. (2002). Role of the lever arm in the processive stepping of myosin V. Proc. Natl. Acad. Sci. USA *99*, 14159–14164.

Rief, M., Rock, R.S., Mehta, A.D., Mooseker, M.S., Cheney, R.E., and Spudich, J.A. (2000). Myosin-V stepping kinetics: a molecular model for processivity. Proc. Natl. Acad. Sci. USA *97*, 9482–9486.

Rock, R.S., Rief, M., Mehta, A.D., and Spudich, J.A. (2000). In vitro assays of processive myosin motors. Methods *22*, 373–381.

Rock, R.S., Rice, S.E., Wells, A.L., Purcell, T.J., Spudich, J.A., and Sweeney, H.L. (2001). Myosin VI is a processive motor with a large step size. Proc. Natl. Acad. Sci. USA *98*, 13655–13659.

Rogat, A.D., and Miller, K.G. (2002). A role for myosin VI in actin dynamics at sites of membrane remodeling during Drosophila spermatogenesis. J. Cell Sci. *115*, 4855–4865.

Roth, K., and Weiner, M.W. (1991). Determination of cytosolic ADP and AMP concentrations and the free energy of ATP hydrolysis in human muscle and brain tissues with 31P NMR spectroscopy. Magn. Reson. Med. *22*, 505–511.

Sakamoto, T., Wang, F., Schmitz, S., Xu, Y., Molloy, J.E., Veigel, C., and Sellers, J.R. (2003). Neck length and processivity of myosin V. J. Biol. Chem. *278*, 29201–29207

Schwaiger, I., Sattler, C., Hostetter, D.R., and Rief, M. (2002). The myosin coiled-coil is a truly elastic protein structure. Nat. Mater. *1*, 232–235.

Sheetz, M., ed. (1998). Laser Tweezers in Cell Biology (Academic Press).

Sheterline, P., and Sparrow, J.C. (1994). Actin. Protein Profile *1*, 1–121.

Spudich, J.A. (2001). The myosin swinging cross-bridge model. Nat. Rev. Mol. Cell Biol. *2*, 387–392.

Stryer, L. (1995). Biochemistry, 4th edn (New York, W.H. Freeman and Company).

Sweeney, H.L., Rosenfeld, S.S., Brown, F., Faust, L., Smith, J., Xing, J., Stein, L.A., and Sellers, J.R. (1998). Kinetic tuning of myosin via a flexible loop adjacent to the nucleotide binding pocket. J. Biol. Chem. *273*, 6262–6270.

Trybus, K.M., Freyzon, Y., Faust, L.Z., and Sweeney, H.L. (1997). Spare the rod, spoil the regulation: necessity for a myosin rod. Proc. Natl. Acad. Sci. USA *94*, 48–52.

Veigel, C., Coluccio, L.M., Jontes, J.D., Sparrow, J.C., Milligan, R.A., and Molloy, J.E. (1999). The motor protein myosin-I produces its working stroke in two steps. Nature *398*, 530–533.

Wang, M.D., Schnitzer, M.J., Yin, H., Landick, R., Gelles, J., and Block, S.M. (1998). Force and velocity measured for single molecules of RNA polymerase. Science *282*, 902–907.

Wells, A.L., Lin, A.W., Chen, L.Q., Safer, D., Cain, S.M., Hasson, T., Carragher, B.O., Milligan, R.A., and Sweeney, H.L. (1999). Myosin VI is an actin-based motor that moves backwards. Nature *401*, 505–508.

Zhuang, X., and Rief, M. (2003). Single-molecule folding. Curr. Opin. Struct. Biol. *13*, 88–97.